Supplementary Information (SI) for EES Batteries.

Supporting Information: Effect of particle size on the slurry-based processability and conductivity of t-Li_7SiPS_8

Duc Hien Nguyen,[a,b] Lars Grunenberg,[a] Igor Moudrakovski,[a] Kathrin Küster,[a] and Bettina V. Lotsch*,[a,b,c]

[a] *Max Planck Institute for Solid State Research, Heisenbergstraße 1, 70569 Stuttgart, Germany*

[b] *LMU Munich, Butenandstraße 5-13, 81377 Munich, Germany*

[c] *Excellence cluster e-conversion, Lichtenbergstraße 4a, 85748 Garching, Germany*

* E-mail: b.lotsch@fkf.mpg.de

Experimentals

Selection of materials

Since tetragonal Li_7SiPS_8 (t-Li_7SiPS_8) belongs to the category of sulfide-based solid electrolytes (SEs), protic solvents are not suitable for processing due to the evolution of hazardous H_2S gas and concomitant material degradation. It was already shown that t-Li_7SiPS_8 has remarkable stability in non-polar solvents with medium to low donor numbers, such as cyclohexane, anisole, toluene, and *p*-xylene.[S1] In this study, anisole, toluene, and *p*-xylene were chosen because of their low to moderate vapor pressures and their industrial compatibility.[S2] Similarly, the selection of binders in this study was based on the absence of protic functional groups, availability, and solubility in the solvents. Therefore, two binders with different chemical structures, polyisobutylene (PIB, fully saturated aliphatic hydrocarbon) and hydrogenated nitrile butadiene rubber (HNBR, -CN functional group), were chosen. An important requirement for the SE separator is the negligible electronic conductivity of the binder. Therefore, chronoamperometric measurements were performed on pure binder films with thicknesses of 100–200 µm. The calculated electronic conductivities were found to be in the range of $10^{-11}\,\mathrm{S\,cm^{-1}}$ and can therefore be neglected.[S3]

Materials

All materials were stored inside an Ar-filled glovebox ($O_2 < 1$ ppm, $H_2O < 1$ ppm, MBraun), and all synthesis and processing steps were performed under an argon atmosphere. Li_2S (99.98%) and Si (99.999%) were supplied by Sigma Aldrich and Alfa Aesar, respectively. Red phosphorous (P, 99%) was purchased from Merck and sulfur (S_8, 99%, sublimed) from Grüssing. Two different hydrogenated nitrile butadiene rubber HNBR-17 ($5.4 \cdot 10^5\,\mathrm{g\,mol^{-1}}$, 17 wt% acetonitrile, < 1% residual double bonds) and HNBR-34 ($2.6 \cdot 10^5\,\mathrm{g\,mol^{-1}}$, 34 wt% acetonitrile, < 1% residual double bonds) were provided by Arlanxeo. Polyisobutylene (PIB, $5 \cdot 10^5\,\mathrm{g\,mol^{-1}}$) was purchased from Sigma Aldrich. Anisole (Sigma-Aldrich, anhydrous, 99.7%), *p*-xylene (Acros, anhydrous, ≥ 99%) and toluene (Acros, extra dry, molecular sieve, 99.85%) were purchased and used, without further purification.

Table S1: Selected binders with their chemical structure and average molecular weight.

Binder	Structure	Average M_W
Polyisobutene (PIB)	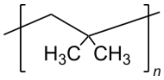	$5 \cdot 10^5\,\mathrm{g\,mol^{-1}}$
Hydrogenated nitrile butadiene rubber (HNBR)	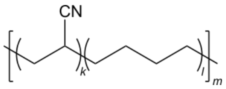	$5.4 \cdot 10^5\,\mathrm{g\,mol^{-1}}$ (HNBR-17) $2.6 \cdot 10^5\,\mathrm{g\,mol^{-1}}$ (HNBR-34)

Table S2: Selected solvents and their chemical structure.

Anisole	*p*-Xylene	Toluene
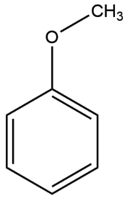	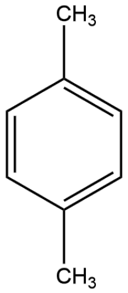	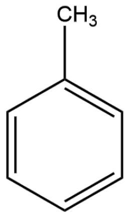

Synthesis of *t*-Li_7SiPS_8

t-Li_7SiPS_8 was obtained from stoichiometric amounts of Li_2S, Si, red phosphorus and sulfur. An excess of 5 wt% sulfur was used to ensure complete oxidation during synthesis. The starting mixture (3 g) was first homogeneously ground, then placed in glassy carbon crucibles and subsequently sealed in a quartz glass ampoule under vacuum ($1 \cdot 10^{-3}$ mbar). The ampoules were transferred to a tube furnace and heated to 525 °C at a rate of $30\,\mathrm{K\,min^{-1}}$, annealed for 100 h, and allowed to cool to ambient temperature. After synthesis, the pale-yellow colored SE powder was ground, then manually sieved using two sieves with mesh sizes of 50 µm 100 µm. The powder fraction that remained in the 100 µm mesh is denoted >100 µm, while the powder that passed the 100 µm mesh but remained on the 50 µm mesh is denoted 50–100 µm. The particle size fraction that passed the 50 µm mesh is denoted <50 µm.

Fabrication of *t*-Li_7SiPS_8 sheets

The binders were dried at 40 °C under dynamic vacuum for at least 48 h inside a drying oven (Büchi B-585) before transfer into the glovebox. The binders were dissolved in the solvents depending on their solubility (Tab. S3), which resulted in six different binder solutions with each containing 10 wt% binder.

Table S3: Compatibility of binders and solvents. Note: Solubility is denoted with "*o*", whereas "–" means insoluble.

	HNBR-17	HNBR-34	PIB
anisole	o	o	–
p-xylene	o	–	o
toluene	o	–	o

Figure S1 shows the unsuccessful preparation of binder stock solutions of HNBR-34 in *p*-xylene and toluene and PIB in anisole due to the insolubility of the binders in the respective solvents and a binder stock solution of HNBR-34 in anisole as a representative for the processable binder stock solutions.

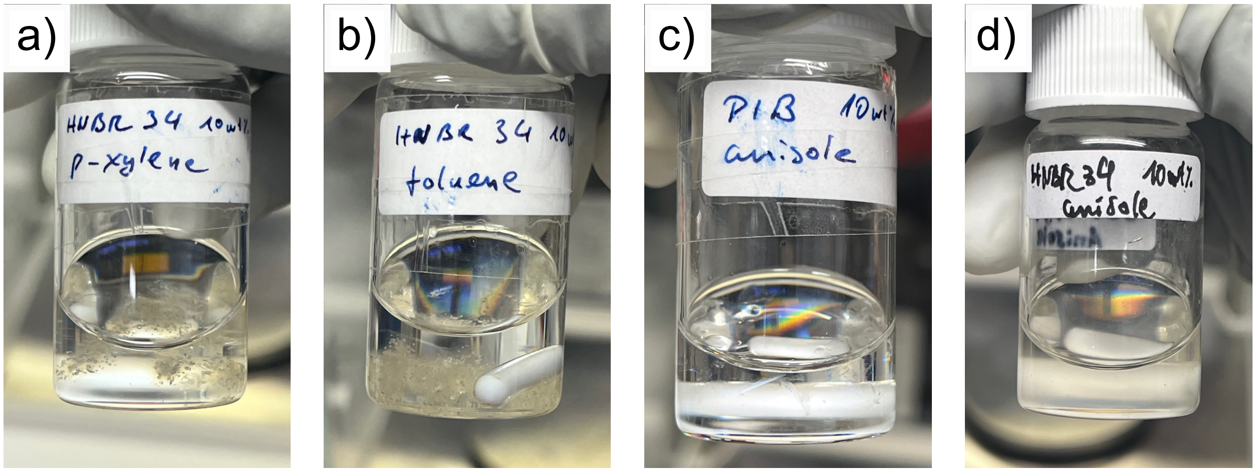

Figure S1: Unsuccessful preparation of binder stock solutions of (a) HNBR-34 in *p*-xylene, (b) HNBR-34 in toluene, (c) PIB in anisole. (d) shows the successful preparation of the binder stock solution of HNBR-34 in anisole.

Among the investigated solvents, anisole is the most polar one with a dielectric constant $\epsilon = 4.3$ and donor number DN = 7.9, followed by toluene ($\epsilon = 2.4$, DN = 3.9) and *p*-xylene ($\epsilon = 2.3$, DN = 4.8)[S4] In the case of the binders, HNBR-34 with a high content of acrylonitrile as a polar functional group (34 wt%, $\epsilon = 38$),[S5] is the most polar one and thus was only soluble in anisole. In contrast, PIB with no functional groups and consisting of hydrocarbons only, is the least polar binder and was only soluble in the low-polarity solvents *p*-xylene and toluene. HNBR-17 with an acrylonitrile content of 17 wt% was soluble in all investigated solvents. A key indicator of the slurry's processability is its viscosity, which can be controlled by the solid content of the slurry. A slurry with a low solid content is characterized by low viscosity and thus will seep out under the applicator, resulting in inhomogeneous sheets. In contrast, a high solid content will result in a slurry too viscous and will stick to the applicator, making proper processing difficult. The best solid content (*i.e.* SE+binder) in the slurry for optimal processability was found to be between 35-50 wt% while maintaining the *t*-Li_7SiPS_8:binder ratio at 90:10 wt% to form mechanically stable sheets. After mixing with a magnetic stirrer overnight, the slurry was coated *via* doctor blading with a 400 µm gap-rod (manufactured in-house) on siliconized polyester foil (PPI Adhesive Products GmbH).

The obtained SE sheets were first slowly dried at room temperature overnight to prevent too rapid solvent evaporation which would leave empty spots. To ensure consistent sheet quality, the sheets were first slowly dried at room temperature overnight. This step is necessary, as in our experience, drying the sheet on a heating plate right after doctor blading usually led to irregularities due to the formation of empty spots within the sheet. We attribute this observation to too rapid solvent evaporation. Over time and after repeated sheet "failures", we included the additional step of slow and soft solvent evaporation by letting the sheet rest at room temperature overnight. Subsequently, they were further dried on a heating plate at 60 °C for at least 24 h to remove left-over solvent and ensure cohesion within the sheets. For all following measurements, the samples were punched out of the sheets using a punching die and transferred into a Büchi drying oven for further drying at 60 °C under dynamic vacuum for at least 48 h. Freestanding SE sheets of approximately 100–150 µm thickness were obtained.

Powder X-ray diffraction

Powder X-ray diffraction (PXRD) measurements were carried out on a STOE Stadi-P diffractometer in Debye-Scherer geometry with Cu-$K_{\alpha 1}$ irradiation (1.5406 Å) and a Ge(111) monochromator. The samples were sealed in borosilicate glass capillaries (⌀ 0.3 mm, Hilgenberg glass no. 14) under argon. For the analysis and Rietveld refinements of the PXRD patterns, TOPAS 6.0 software was used.[S6]

Scanning Electron Microscopy and Energy-dispersive X-ray Spectroscopy

Scanning electron microscopy (SEM) images were taken with a Vega4 LMU microscope (Tescan) and energy dispersive X-ray spectroscopy (EDX) maps were recorded with an Oxford X-Max^{N} 20 EDX-detector.

X-ray photoelectron spectroscopy

X-ray photoelectron spectroscopy (XPS) data were acquired in a Kratos Axis Ultra system (base pressure of at least $5 \cdot 10^{-10}$ mbar) equipped with a monochromated Al-$K_{\alpha 1}$ X-ray source 1486.6 eV. A pass energy of 20 eV was used for high-resolution spectra. Although no charge neutralization was used, an overall binding energy shift of the spectra due to slight surface charging was noticed. Therefore, the binding energy was calibrated by setting the C 1s binding energy to 284.4 eV.[S7] As some changes in the peak shapes were observed during the measurement, several separate spectra of C 1s, S 2p, P 2p, and Si 2p with a few scans were recorded. The spectra with no changes in shape were summed up to improve the signal-to-noise ratio. The samples were screwed onto the sample holder inside the glovebox. For the transfer between the glovebox and the XPS system, the samples were kept in an airtight transfer tool under a protective argon atmosphere. The data was analyzed using CasaXPS.[S8] For fitting, a Shirley background was subtracted, and for S 2p, P 2p, and Si 2p the doublet separation was constrained to 1.18 eV, 0.84 eV and 0.6 eV, respectively. The area ratio was constrained to 2:1.

Solid-state nuclear magnetic resonance spectroscopy

Solid-state nuclear magnetic resonance (ss-NMR) measurements were conducted on a Bruker Avance-III 400 MHz wide bore instrument in a magnetic field of $B_0 = 9.4\,T$. The samples were flame-sealed in pyrex magic-angle spinning (MAS) inserts for Bruker 4 mm rotors (Wilmad Glass, product # DWGSK2576-1). ^{31}P, ^{7}Li and ^{29}Si MAS spectra recorded in 4 mm zirconia rotors at a spinning speed of 10 kHz using a Bruker BL4 MAS probe. A simple Bloch decay excitation scheme was used with a total of 512-4096 accumulations in each experiment. The relaxation delay was set long enough to allow for complete relaxation of the magnetization and a quantitative measurement. The ^{31}P, ^{7}Li and ^{29}Si spectra were directly referenced to 85% H_3PO_4, LiCl and trimethylsilane (TMS), respectively.

^{7}Li pulsed-field-gradient NMR

^{7}Li pulsed-field-gradient nuclear magnetic resonance (PFG-NMR) diffusion measurements were conducted on a Bruker Avance III 400 MHz instrument equipped with a diff60 gradient probe. Data was acquired using a stimulated echo sequence with diffusion times in the range of 25 ms to 150 ms and effective gradient durations of 1 ms to 3 ms. The measured series of gradient attenuated echo-signals were phase corrected, and the integrated areas were used to extract the diffusion coefficients, using the Topspin 3.5 Dynamics module.

Electrochemical impedance spectroscopy

Electrochemical impedance spectroscopy (EIS) was performed to determine the ionic conductivity of the samples. Pristine t-Li_7SiPS_8 powder was uniaxially cold pressed with a force of 500 MPa for 3 min, resulting in a compacted pellet (⌀ 5 mm) of about 2 mm thickness. For the t-Li_7SiPS_8 sheets, three circular discs (⌀ 8 mm) were stacked on top of each other and their thickness was determined after the measurement. During the measurement, an operating cell pressure of 4 MPa was applied. The impedance spectra (1 MHz-1 Hz, root mean square AC voltage of 25 mV) were recorded at room temperature on a NEISYS novocontrol in a two-electrode setup using a Microcell HC cell stand loaded with TSC Battery cell (both from rhd instruments). The analysis of the spectra was performed on RelaxIS3 from rhd instruments. For the fitting process, the data points were proportionally weighted and the frequency range was adjusted to 1 MHz to 1 kHz. Adjustments to the frequency range were necessary for some samples to obtain meaningful fits. For each sample series, EIS on triplicates were performed and evaluated.

SEM and EDX mapping of t-Li_7SiPS_8 sheets

Figure S2 shows the morphology of processed t-Li_7SiPS_8 sheets (50 µm with different binders and solvents. At higher magnifications (middle row), similar rough microstructures for all processed sheets are observed. The bottom row depicts the EDX map of carbon in the sheets. As the binder is the only carbon source, the mapping provides a qualitative representation of its distribution within the sheets.

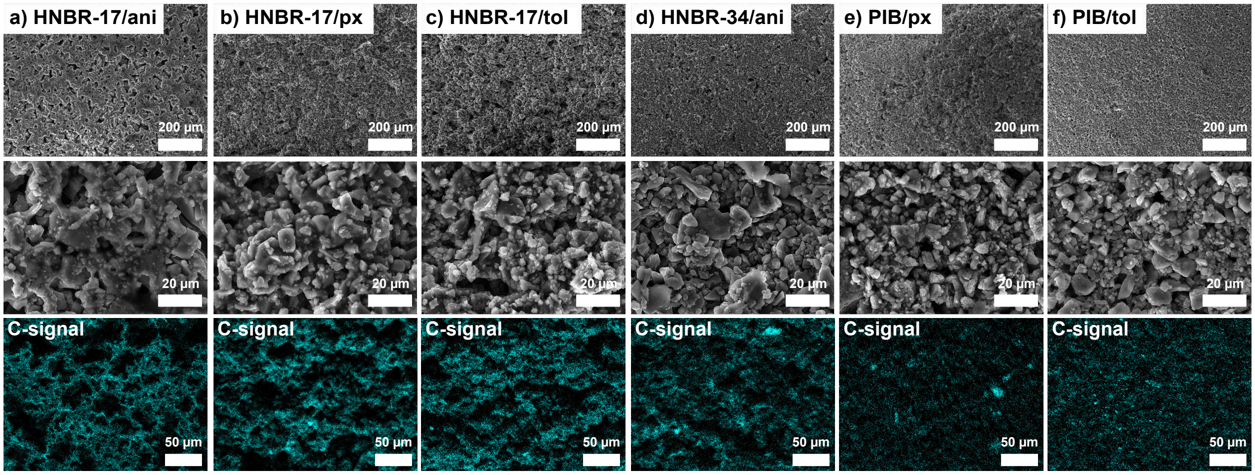

Figure S2: SEM images (top and middle row) of t-Li_7SiPS_8 sheets processed with: (a) HNBR-17 in anisole, (b) HNBR-17 in p-xylene,(c) HNBR-17 in toluene, (d) HNBR-34 in anisole, (e) PIB in p-xylene, and (f) PIB in toluene, and their corresponding EDX-maps (bottom row) of the C-signal as an indicator for the binder distribution within the sheets. The depicted sheets were fabricated from the fraction having a particle size distribution of <50 µm and a SE:binder ratio of 90:10 wt%.

Figure S3 depicts EDX elemental maps of the remaining elements (top row: sulfur, middle row: phosphorus, bottom row: silicon) of the t-Li_7SiPS_8 sheets. Independent of the slurry formulation, a homogeneous distribution of the elements is observed in general. Incorporating PIB as the binder (Fig. S3e,f) leads to less rough-looking surfaces compared to the other binders. In the Si maps, brighter spots can be observed in some cases (Fig. S3a,b,d), which were identified to be SiO_2 impurities likely originating from partial oxidation of the raw material.

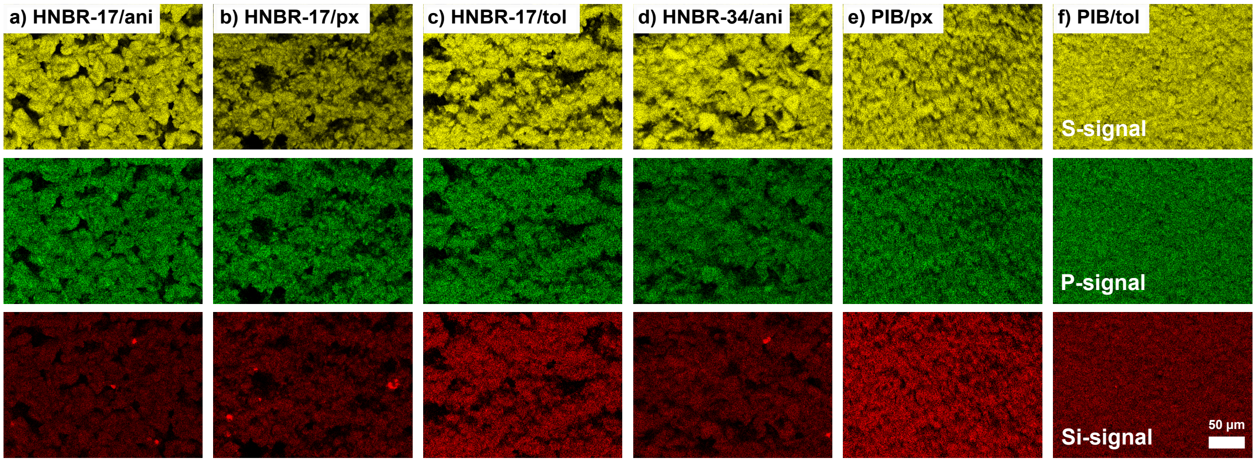

Figure S3: Abbreviations used in the figure: ani stands for anisole, px for *p*-xylene, and tol for toluene. EDX maps of S-signal (top row), P-signal (middle row) and Si-signal (bottom row) of *t*-Li_7SiPS_8 sheets processed with: (a) HNBR-17 in anisole, (b) HNBR-17 in *p*-xylene, (c) HNBR-17 in toluene, (d) HNBR-34 in anisole, (e) PIB in *p*-xylene and (f) PIB in toluene. The depicted sheets consist of particle sizes <50 µm.

Comparison of unsieved and sieved t-Li$_7$SiPS$_8$ powder fractions *via* SEM

In this section unsieved t-Li$_7$SiPS$_8$ powder (Fig. S4a) is qualitatively compared to its sieved fractions (Fig. S4b-d) *via* SEM. Although the unsieved t-Li$_7$SiPS$_8$ powder was finely dispersed on the SEM sample holder and appears homogeneous at low magnifications, several larger agglomerates are observed. At high magnifications, it can be seen that the morphology is similar for unsieved and sieved powder and that the particles consist of agglomerates.

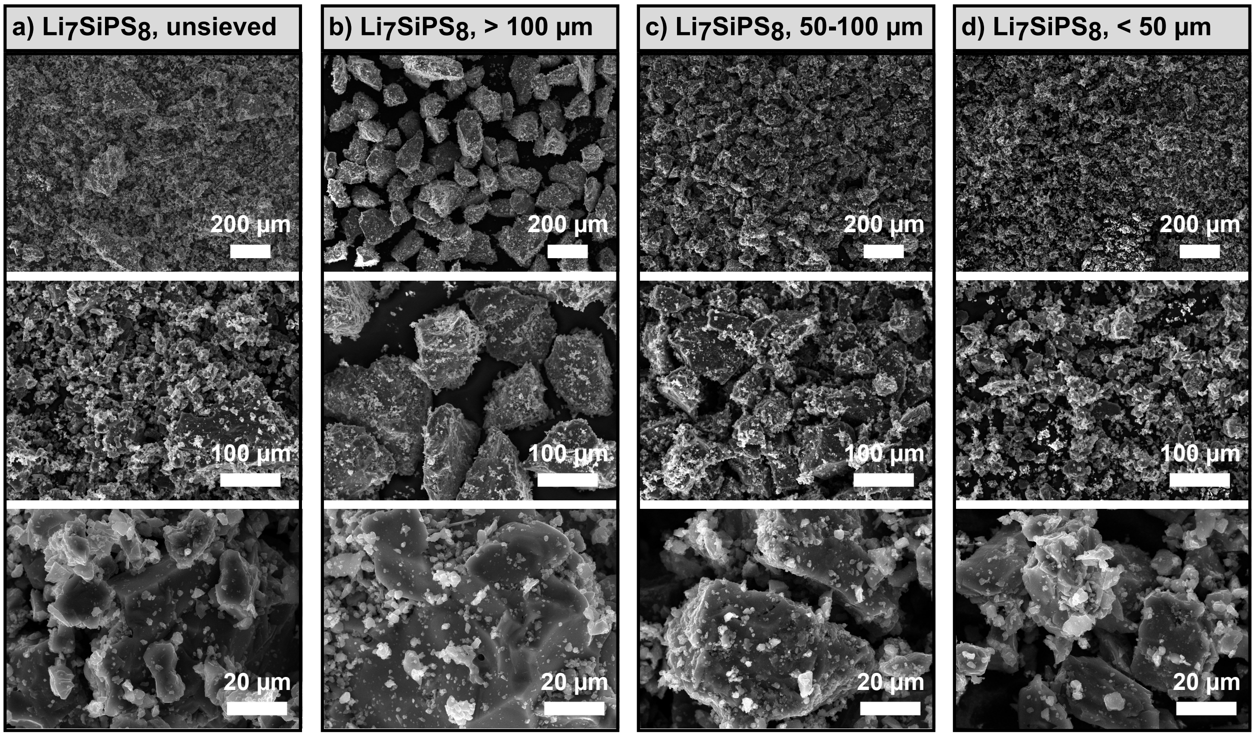

Figure S4: Top-view SEM images of (a) unsieved and (b)-(d) sieved fractions of t-Li$_7$SiPS$_8$ particles with different mesh sizes leading to different particle size distributions: >100 µm, 50–100 µm and <50 µm.

^{7}Li / ^{29}Si MAS NMR and XPS of t-$\mathrm{Li_7SiPS_8}$ sheets

^{7}Li and ^{29}Si MAS NMR (Fig. S5a and b, respectively) were conducted on the sheets processed with HNBR-17 in every solvent combination and compared to the pristine sample. No peak shift or additional features are observed after slurry-based processing. Additionally, XPS in the Si 2p region was performed and is summarized in Figure S5c-f. The orange peaks (100.8–101.7 eV) are attributed to $\mathrm{SiS_4}^{4-}$ units while the green peaks are assigned to silicone or siloxane (101.5–103.3 eV)^{S9} as trace impurities.

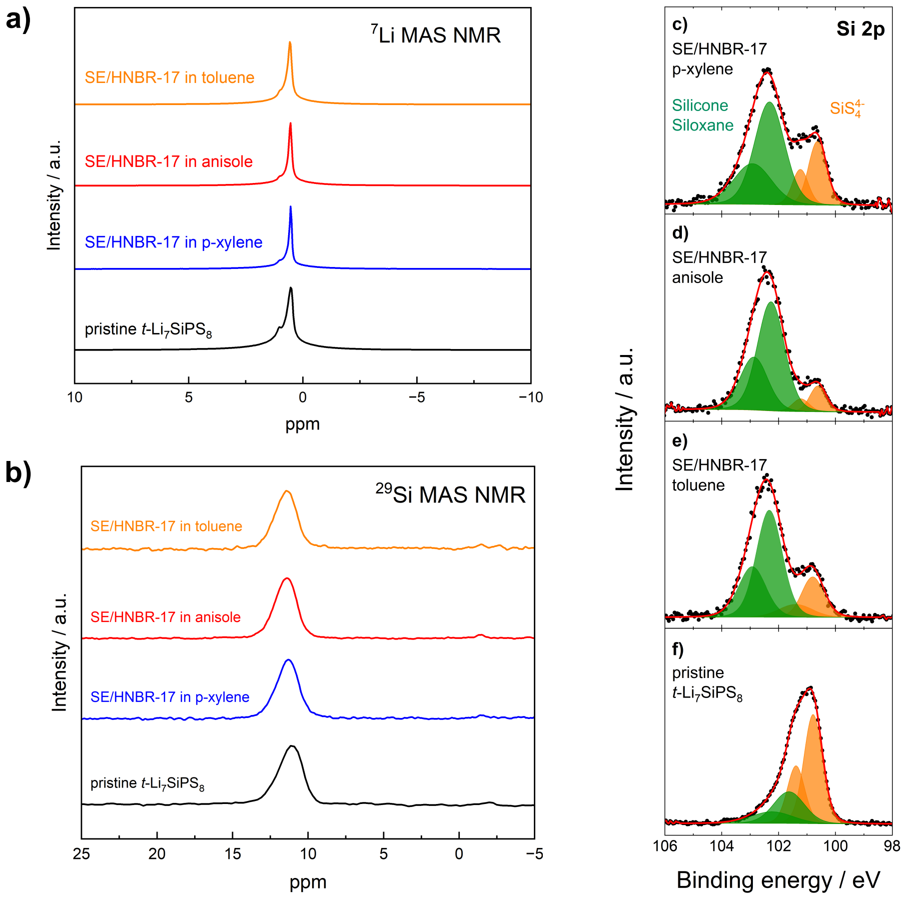

Figure S5: (a) ^{7}Li and (b) ^{29}Si MAS NMR of sheets processed with HNBR-17 in toluene, anisole, and p-xylene and of pristine t-$\mathrm{Li_7SiPS_8}$ powder. XPS signals in the Si 2p region of the sheets processed with HNBR-17 (c) in p-xylene, (d) in anisole, (e) in toluene and (f) pristine t-$\mathrm{Li_7SiPS_8}$ powder.

Fitting of EIS spectra

The Nyquist plot of the pristine sample shows a polarization line that is modeled with a serial arrangement of the circuit elements resistor (R) and constant phase element (CPE) as shown in Figure S6. The intercept of R with the x-axis includes contributions from the bulk and intraparticle grain boundary resistances for the ion transport which cannot be deconvoluted at room temperature.[S10–S12] The CPE represents the capacitive behavior of the solid ionic conductor in the form of electrode polarization when in contact with an ionically blocking electrode (stainless steel). The Nyquist plots of the sheets exhibit a semi-circle at high frequencies and a low-frequency polarization tail, described by a parallel arrangement of R and CPE and a serial CPE, respectively. When the CPE is modeled in parallel to R, the effective capacitance (C_{eff}) associated with the transport properties of the material can be calculated by using the Brug formula:

$$C_{eff} = Q^{(1/\alpha)} \cdot R^{(1/\alpha - 1)}, \tag{1}$$

where Q corresponds to the admittance of CPE and α is the exponential factor.[S13] The obtained capacitances are in the nanofarad (nF) range and are thus attributed to the grain boundary properties of t-Li_7SiPS_8. By multiplying the inverse of$R$ with the fraction of the sample thickness (t) and area (A), the (ionic) conductivity (σ) is obtained via:

$$\sigma = \frac{1}{R} \cdot \frac{t}{A}. \tag{2}$$

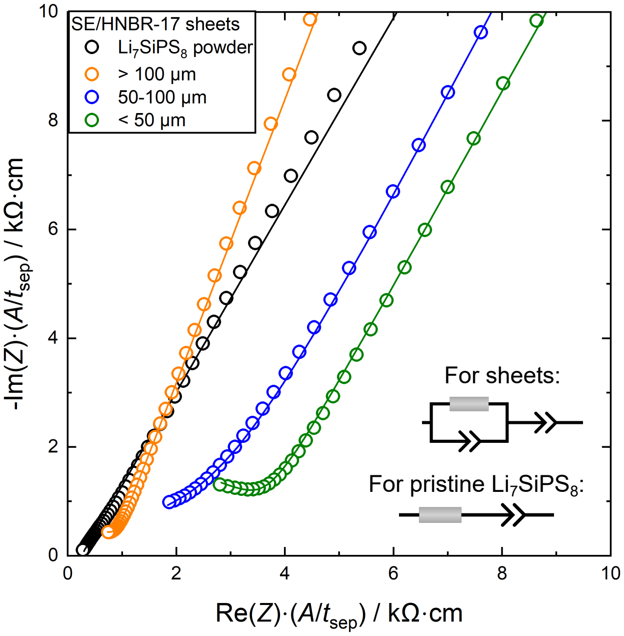

Figure S6: (a) Exemplary Nyquist plots of pristine t-Li_7SiPS_8 powder (black) and t-Li_7SiPS_8 sheets (with HNBR-17 in toluene) consisting of $>$100 µm (orange), 50–100 µm (blue) and $<$50 µm (green) particle size distributions. The Nyquist plots were normalized to the area and sample thickness.

Qualitative analysis of *t*-Li_7SiPS_8 sheets before and after EIS measurement via SEM

Figure S7 qualitatively compares exemplary *t*-Li_7SiPS_8 sheets (HNBR-17 in toluene) comprised of particle size fractions >100 µm (Fig. S7a), 50–100 µm (Fig. S7b) and <50 µm (Fig. S7c) before EIS (uncompressed, left side) and after EIS (compressed, right side) measurements *via* SEM. Note that the sample sheets were compressed at 4 MPa during EIS measurement leading to changes in morphologies before and after EIS measurements. Aggregates appear to fracture into smaller particles after the EIS measurements due to the applied contact pressure during the experiment. This is particularly evident in the sheet consisting of >100 µm particles. The intergranular voids are filled by broken particles, which increase the homogeneity of the sheet and enable better intergranular contacts. In contrast, the sheets composed of smaller-sized particles are already homogeneous in the uncompressed state. Here, the applied pressure seems to separate the grains from each other. This is especially apparent in the case of the sheet made of <50 µm particles where a significant amount of intergranular voids are observed after EIS measurements, hinting at increased fracturing.

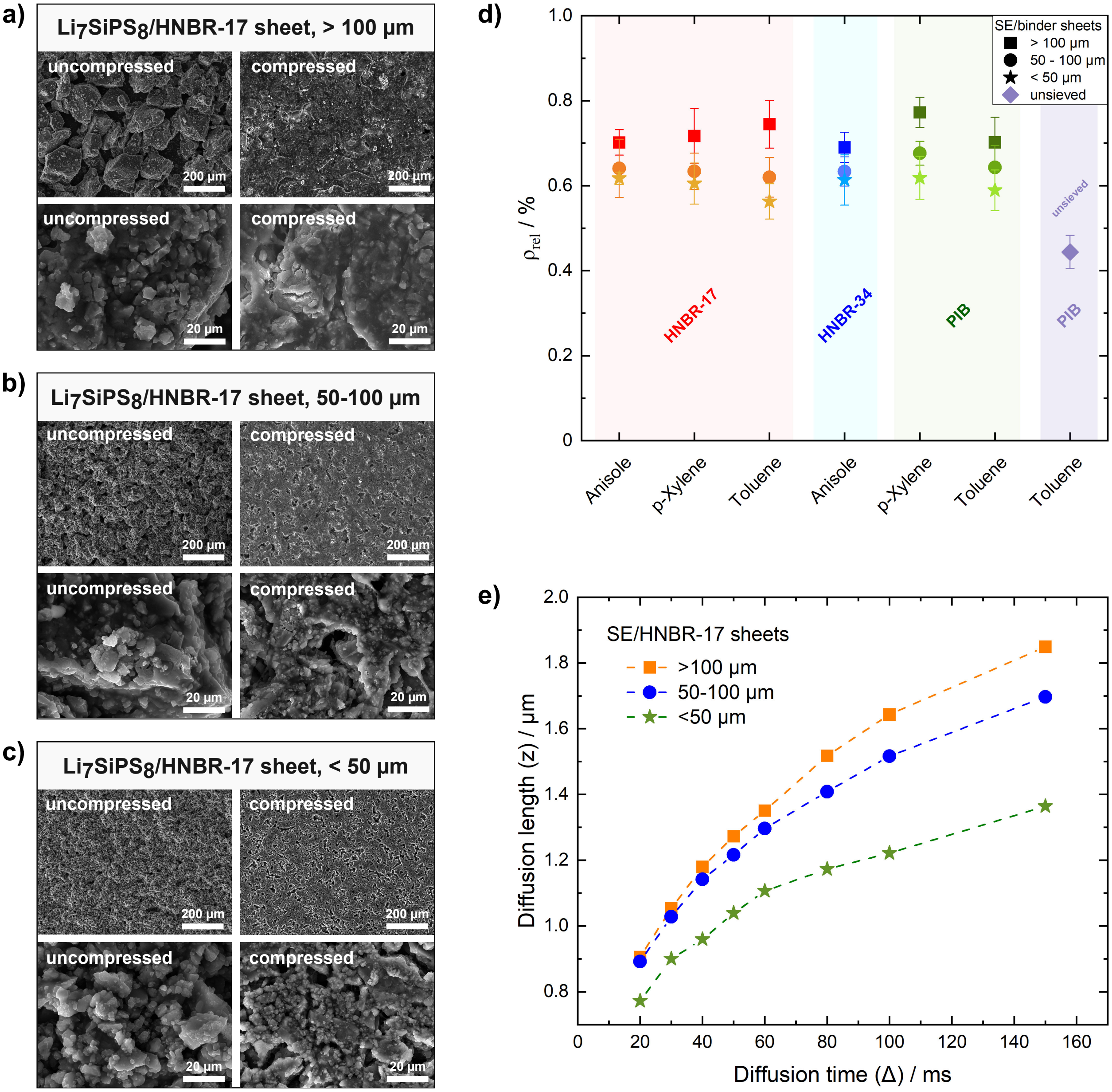

Figure S7: SEM images of exemplary *t*-Li_7SiPS_8 sheets (HNBR-17 in toluene) consisting of (a) >100 µm, (b) 50–100 µm and (c) <50 µm particle sizes in the uncompressed (before EIS measurement, left) and compressed (after EIS measurement, right) state. (d) Relative densities of *t*-Li_7SiPS_8/binder sheets of different slurry formulations (red: HNBR-17, blue: HNBR-34, green: PIB in their respective solvents) and different particle sizes. The relative density of an exemplary sheet (PIB in toluene) consisting of unsieved *t*-Li_7SiPS_8 particles (purple) is also shown for comparison. (e) Diffusion length as a function of diffusion time as obtained by ^{7}Li PFG NMR measurements of *t*-Li_7SiPS_8 sheets (with HNBR-17 in toluene) comprised of different particle sizes.

Relative density calculation after EIS measurement

To estimate the relative density (ρ_{rel}) of the sheets after EIS measurements, we used the following equation

$$\rho_{rel} = \frac{\rho_{exp}}{\rho_{theo}} \tag{3}$$

where ρ_{exp} is the experimentally calculated density for each sheet. ρ_{theo} is the theoretical density, derived from the sum of bulk densities of the binder and *t*-Li_7SiPS_8 and considering their weight fractions in the respective sheets. For *t*-Li_7SiPS_8 the crystallographic density of 1.923(9) $g\,cm^{-3}$ was used.[S14] For the different binders, the bulk densities were taken from the product specification sheet (PIB: 0.92 $g\,cm^{-3}$ and HNBR: 0.96 $g\,cm^{-3}$). Figure S7d shows the relative densities of the sheets consisting of different particle sizes after EIS measurements (after compression). While the relative density values within a certain formulation are very similar, sheets consisting of >100 µm particles tend to have the highest values, of around 70-75%. In comparison, sheets made of <50 µm particles show lower relative densities between 60-65%. These observations are consistent with the visual analysis made in Figure S7a-c. Interestingly, the exemplary sheet (with PIB and toluene) comprised of unsieved *t*-Li_7SiPS_8 particles shows the lowest calculated relative density of about 45%, which can be increased by applying higher operating pressures as shown in previous reports.[S15,S16]

References

(S1) Hatz, A.-K.; Calaminus, R.; Feijoo, J.; Treber, F.; Blahusch, J.; Lenz, T.; Reichel, M.; Karaghiosoff, K.; Vargas-Barbosa, N. M.; Lotsch, B. V. Chemical stability and ionic conductivity of LGPS-type solid electrolyte tetra-Li_7SiPS_8 after solvent treatment. ACS Applied Energy Materials **2021**, 4, 9932–9943.

(S2) Yamamoto, M.; Takahashi, M.; Terauchi, Y.; Kobayashi, Y.; Ikeda, S.; Sakuda, A. Fabrication of composite positive electrode sheet with high active material content and effect of fabrication pressure for all-solid-state battery. Journal of the Ceramic Society of Japan **2017**, 125, 391–395.

(S3) Riphaus, N.; Strobl, P.; Stiaszny, B.; Zinkevich, T.; Yavuz, M.; Schnell, J.; Indris, S.; Gasteiger, H. A.; Sedlmaier, S. J. Slurry-based processing of solid electrolytes: a comparative binder study. Journal of The Electrochemical Society **2018**, 165, A3993–A3999.

(S4) Linert, W.; Fukuda, Y.; Camard, A. Chromotropism of coordination compounds and its applications in solution. Coordination Chemistry Reviews **2001**, 218, 113–152.

(S5) Ineos Acrylonitrile Safe Storage and Handling Guide. `https://www.ineos.com/globalassets/ineos-group/businesses/ineos-nitriles/she/acrylonitrile_brochure.pdf` [Accessed: (10.04.2025)].

(S6) Coelho, A. A. TOPAS and TOPAS-Academic: an optimization program integrating computer algebra and crystallographic objects written in C++. Journal of Applied Crystallography **2018**, 51, 210–218.

(S7) Biesinger, M. C. Accessing the robustness of adventitious carbon for charge referencing (correction) purposes in XPS analysis: Insights from a multi-user facility data review. Applied Surface Science **2022**, 597, 153681.

(S8) Fairley, N.; Fernandez, V.; Richard-Plouet, M.; Guillot-Deudon, C.; Walton, J.; Smith, E.; Flahaut, D.; Greiner, M.; Biesinger, M.; Tougaard, S.; others Systematic and collaborative approach to problem solving using X-ray photoelectron spectroscopy. Applied Surface Science Advances **2021**, 5, 100112.

(S9) Riegger, L. M.; Otto, S.-K.; Sadowski, M.; Jovanovic, S.; Kötz, O.; Harm, S.; Balzat, L. G.; Merz, S.; Burkhardt, S.; Richter, F. H.; others Instability of the Li_7SiPS_8 Solid Electrolyte at the Lithium Metal Anode and Interphase Formation. Chemistry of Materials **2022**, 34, 3659–3669.

(S10) Irvine, J. T.; Sinclair, D. C.; West, A. R. Electroceramics: characterization by impedance spectroscopy. Advanced materials **1990**, 2, 132–138.

(S11) Kraft, M. A.; Culver, S. P.; Calderon, M.; Böcher, F.; Krauskopf, T.; Senyshyn, A.; Dietrich, C.; Zevalkink, A.; Janek, J.; Zeier, W. G. Influence of lattice polarizability on the ionic conductivity in the lithium superionic argyrodites Li_6PS_5X (X= Cl, Br, I). Journal of the American Chemical Society **2017**, 139, 10909–10918.

(S12) Ohno, S.; Bernges, T.; Buchheim, J.; Duchardt, M.; Hatz, A.-K.; Kraft, M. A.; Kwak, H.; Santhosha, A. L.; Liu, Z.; Minafra, N.; others How certain are the reported ionic conductivities of thiophosphate-based solid electrolytes? An interlaboratory study. ACS Energy Letters **2020**, 5, 910–915.

(S13) Brug, G.; van den Eeden, A. L.; Sluyters-Rehbach, M.; Sluyters, J. H. The analysis of electrode impedances complicated by the presence of a constant phase element. Journal of electroanalytical chemistry and interfacial electrochemistry **1984**, 176, 275–295.

(S14) Harm, S.; Hatz, A.-K.; Moudrakovski, I.; Eger, R.; Kuhn, A.; Hoch, C.; Lotsch, B. V. Lesson learned from NMR: characterization and ionic conductivity of LGPS-like Li_7SiPS_8. Chemistry of Materials **2019**, 31, 1280–1288.

(S15) Sedlmeier, C.; Kutsch, T.; Schuster, R.; Hartmann, L.; Bublitz, R.; Tominac, M.; Bohn, M.; Gasteiger, H. A. From Powder to Sheets: A Comparative Electrolyte Study for Slurry-Based Processed Solid Electrolyte/Binder-Sheets as Separators in All-Solid-State Batteries. Journal of The Electrochemical Society **2022**, 169, 070508.

(S16) Tron, A.; Hamid, R.; Zhang, N.; Paolella, A.; Wulfert-Holzmann, P.; Kolotygin, V.; López-Aranguren, P.; Beutl, A. Film processing of Li_6PS_5Cl electrolyte using different binders and their combinations. Journal of Energy Storage **2023**, 66, 107480.